Initial scalar lithospheric magnetic anomaly map of China and surrounding regions derived from CSES satellite data

Journal:	*Science China Technological Sciences*
Manuscript ID	SCTS-2020-0800.R2
Manuscript Type:	Original Article
Date Submitted by the Author:	11-Sep-2020
Complete List of Authors:	Wang, Jie; National Institute of Natural Hazards, Ministry of Emergency Management of China; School of Space and Environment, Beihang University Shen, Xuhui ; National Institute of Natural Hazards, Ministry of Emergency Management of China yang, yanyan; National Institute of Natural Hazards, Ministry of Emergency Management of China Zeren, Zhima; National Institute of Natural Hazards, Ministry of Emergency Management of China Hulot, Gauthier; Université de Paris, Institut de physique du globe de Paris, CNRS Olsen, Nils; DTU Space, National Space Institute, Technical University of Denmark Zhou, Bin; National Space Science Center Chinese Academy of Sciences Magnes, Werner; Space Research Institute, Austrian Academy of Sciences De Santis, Angelo; Istituto Nazionale di Geofisica e Vulcanologia, Via di Vigna Murata huang, jianping; National Institute of Natural Hazards, Ministry of Emergency Management of China Guo, Feng; National Institute of Natural Hazards, Ministry of Emergency Management of China Liu, Wenlong; School of Space and Environment, Beihang University Yu, Jingbo; Hebei GEO University
Keywords:	Lithospheric magnetic anomaly, CSES, Satellite magnetic anomaly, Long-wavelength magnetic anomaly
Speciality:	Space Sciences

Note: The following files were submitted by the author for peer review, but cannot be converted to PDF. You must view these files (e.g. movies) online.
Figure 1.srf Figure 2.wmf Figure 3.srf Figure 4.srf Figure 5.srf Figure 6.srf

Initial scalar lithospheric magnetic anomaly map of China and surrounding regions derived from CSES satellite data

Jie Wang[1,2], Xuhui Shen[1]*, Yanyan Yang[1], Zhima Zeren[1], Gauthier Hulot[3], Nils Olsen[4], Bin Zhou[5], Magnes Werner[6], Angelo De Santis[7], Jianping Huang[1], Feng Guo[1], Wenlong Liu[2], Jingbo Yu[8]

1 National Institute of Natural Hazards, Ministry of Emergency Management of China, Beijing, 100085, China

2 School of Space and Environment, Beihang University, Beijing, 100191, China

3 Université de Paris, Institut de physique du globe de Paris, CNRS, F-75005 Paris, France

4 DTU Space, National Space Institute, Technical University of Denmark, 2800 Kongens Lyngby, Denmark

5 National Space Science Center, Chinese Academy of Sciences, Beijing, 100190, China

6 Space Research Institute, Austrian Academy of Sciences, Graz, 8042, Austria

7 Istituto Nazionale di Geofisica e Vulcanologia, Via di Vigna Murata, 605 Rome, Italy

8 Heibei Geo University, Shijiazhuang, 050031, China

Abstract

The China Seismo-Electromagnetic Satellite (CSES), China's first satellite to measure geophysical fields with scientific goals in both space and solid earth physics, was launched successfully in February 2018. It carries high-precision magnetometers to measure the geomagnetic field. In this study, the CSES magnetic data were used to extract the signal of the lithospheric magnetic field caused by magnetized rocks in the crust and uppermost mantle. First, an along-track analysis of the CSES magnetic data was undertaken near the Bangui magnetic anomaly in central Africa and the Tarim magnetic anomaly in China, demonstrating that the CSES magnetic data are indeed sensitive to the lithospheric magnetic anomaly field. Then a lithospheric magnetic anomaly map over China and surrounding regions was derived. This map is consistent with the lithospheric part of the CHAOS-7 model. In particular, it clearly reveals four major magnetic anomalies containing long-wavelength signals at the altitude of Low-Earth-Orbiting satellites. Three magnetic highs are located over the Tarim, Sichuan and Songliao basin, the origins of which could be related to large-scale tectonic-magmatic activities during geological history. A prominent magnetic low is otherwise found in the southern Himalayan-Tibetan plateau, possibly caused by the shallow Curie depth in this region. To further improve the precision of the lithospheric magnetic field model, more detailed data processing and multi-source data merging are needed.

Keywords Lithospheric magnetic anomaly, CSES, Satellite magnetic anomaly, Long-wavelength magnetic anomaly

1 . Introduction

Lithospheric magnetic anomalies are due to highly magnetized rocks in the crust and the uppermost mantle [1, 2]. They generally are of geological origin and play an important role in understanding crustal evolution [3-5]. At the altitude of Low-Earth-Orbiting satellites, the amplitude of lithospheric magnetic anomalies only reaches tens of nT due to the distance from the sources. These lithospheric magnetic signatures are much weaker than the Earth's core field and of the same magnitude as the external field during geomagnetic quiet conditions. Recovering lithospheric magnetic anomalies from satellite magnetic data is mainly a signal-to-noise problem [6]. All magnetic field signals of non-geological origins should first be removed and this calls for accurate magnetic data,

high-precision geomagnetic models and effective processing algorithms. Therefore, the possibility of detecting weak lithospheric magnetic anomaly from a given satellite data set is also a good indicator of the quality of this data.

Magnetic scalar data from the POGO (1967-1971) satellite series, over an altitude range of 400-1500 km, were the first data used to confirm that the weak lithospheric magnetic anomalies can be detected at satellite altitude. A first global magnetic anomaly map was derived by Regan et al. [7]. The Magsat (1979-1980) satellite came next and was the first equipped with both vector and scalar magnetometers. Its data were used to produce global vector and scalar magnetic anomaly maps for geophysical studies [1,6,8]. After Magsat, the Danish Ørsted satellite (1999-2013) was the first mission with similar high-precision magnetic field instruments. It confirmed both the findings of Magsat and the mainly induced nature of the large-scale lithospheric magnetization [9]. It was soon followed by the German CHAMP (CHAllenging Minisatellite Payload) satellite (2000-2010), which delivered continuous magnetic data for ten years. These proved particularly interesting for lithospheric field studies due to the low altitude of the satellite, which ranged from 300 to 454 km. Indeed, lithospheric field models derived from CHAMP data have been widely used for geological interpretations [10-13]. Since November 2013, the Swarm satellite constellation has taken over. Operated by ESA, it comprises three identical satellites [14] and various high-quality lithospheric field models have already been derived from its data (e.g. [15,16]).

The CSES (also called Zhangheng-1, ZH-1) satellite was launched successfully in February 2018 and is China's first satellite to measure geophysical fields with scientific goals of interest to both space and solid earth physics [17,18]. The design lifetime of the satellite system is five years. The payload includes vector and scalar magnetometers to measure the Earth's magnetic field. These data have already been used to produce a global geomagnetic field model (the CSES Global Geomagnetic field Model, CGGM, [19]) which contributed to the determination of the latest IGRF-13 model, together with eleven other candidate models. In the present study, we focus on the lithospheric magnetic anomalies recovered from CSES data. First, the capability of CSES for detecting lithospheric magnetic anomalies is demonstrated by a detailed along-track analysis of data from the Bangui magnetic anomaly in central Africa and the Tarim magnetic anomaly in China. Then a lithospheric magnetic anomaly map of the Chinese region is obtained. This map is found to be in good agreement with the lithospheric part of the CHAOS-7 model [20].

2 . Basic information

2.1 Sources of geomagnetic field

At the altitude of Low-Earth-Orbiting satellites, the Earth's magnetic field intensity ranges from ~20,000 nT near the equator to ~70,000 nT near the poles. It originates from four major sources: (1) the core field, caused by electrical currents in the liquid outer core and representing more than 98% of the total magnetic field at Earth's surface, (2) the external field, produced by currents in the ionosphere and magnetosphere, (3) the lithospheric field, generated by magnetized rocks in the crust and the uppermost mantle at depths shallower than the Curie depth, and (4) the field induced by external field variations in the crust and upper mantle due to their electrical conductivity, which is the smallest among all contributions and is often neglected [15,21].

2.2 Orbit trajectory of CSES

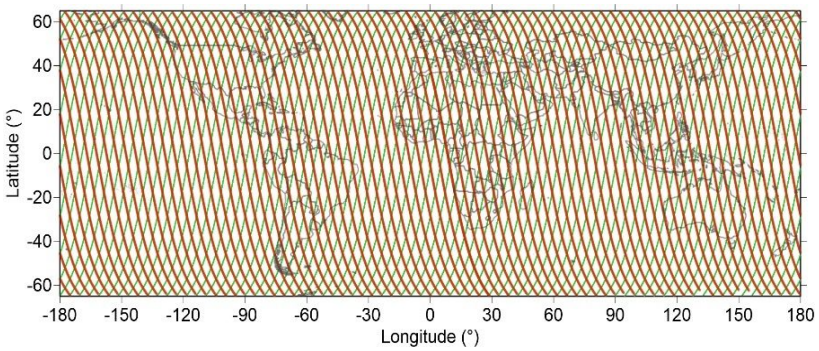

Figure 1 CSES orbit traces during one global revisiting period of 5 days (1 to 5 August 2019). Red curves: night-side orbits with descending node at local time 2:00; green curves: day-side orbits with ascending node at local time 14:00.

The CSES satellite is on a nearly circular near-polar sun-synchronous orbit with an inclination angle of 97.4°. It orbits at a mean altitude of ~507 km above a sphere of radius 6371.2 km with a velocity of 7.6 km/s and a revisiting period of 5 days [17]. The CSES satellite needs about 76 consecutive orbits to provide a global coverage (Figure 1), resulting in an orbit interval of 360°/76≈4.7°. Each orbit can be divided into two half-orbits, night-side (descending node at local time 2:00) and day-side (ascending node at local time 14:00). In Figure 1, the spatial distribution of night-side orbits is shown in red, and that of day-side orbits in green.

2.3 Magnetometers on CSES

The CSES payload includes two types of high precision magnetometer (HPM), including two fluxgate magnetometers (FGM) and a coupled dark state absolute scalar magnetometer (CDSM), with a data sampling rate of 1Hz. The FGM measures the vector magnetic field along three orthogonal components. The CDSM measures the scalar magnetic field intensity with a higher accuracy than the FGM and with absolute stability. It thus is also used for the calibration of the FGM vector data. The accuracy of CDSM is 0.19 nT [22,23]. On-ground prelaunch test showed that the remaining magnetic interference of the platform at the center of the CDSM sensor is lower than 0.33 nT [24]. After temperature correction, absolute value correction and elimination of platform interference, the accuracy of the magnetic field intensity observations was estimated to be within 0.5 nT [25,26].

3 . Data processing

To isolate the lithospheric anomaly field, magnetic contributions from other sources, including the core and external field, have to be removed from the measurements. At the altitude of CSES, the lithospheric field is much weaker than the core field and of similar amplitude as the external field during geomagnetic quiet periods. However, during intense geomagnetic storms, the amplitude of external field reaches hundreds of nT, which is much larger than the lithospheric field signature. Thus, to study the lithospheric magnetic field, only scalar data from magnetic quiet times are selected and processed. Figure 2 shows the data processing procedure of the CSES scalar magnetic data we used.

3.1 Data selection

The satellite magnetic data processing begins with scalar data selection at magnetic quiet times. Ravat et al. [6] proposed to select data according to the K_p geomagnetic activity index for equatorial and mid-latitude regions, and used a cutoff criterion of $K_p < 2+$ for Magsat scalar data. Maus et al. [11] used $K_p \leq 2$ when dealing with the

low-latitude CHAMP scalar data. Thébault et al. [15] used data selection based on the K_p, D_{st} (disturbance storm time index) and IMF (interplanetary magnetic field) indexes for their processing of Swarm data. They selected data only when the hourly D_{st} is such that $|D_{st}| < 5$ nT with variations lower than 5 nT over the three previous hours, K_p is such that $K_p \leq 2-$ in the previous three hour time interval, and IMF values satisfy |IMFBy|<2 nT and IMFBz>0. The CHAOS-7 [20] lithospheric field (identical to the LCS-1 model of Olsen et al. [16] for spherical harmonic degrees above n=20) is derived from CHAMP and Swarm magnetic data for which $K_p \leq 3o$ and the time change of RC (an index similar to D_{st} describing the strength of the magnetospheric ring current) does not exceed 3 nT/hr.

At low latitudes, the influence of ionospheric currents mainly occurs in the day time, so it can be almost entirely avoided by selecting night time data [11]. Here, we only use night-side (descending node at local time 2:00) data, with the additional requirement that $K_p < 2-$, to reduce the influence of external fields.

3.2 Core field removal

Power spectrum analysis indicates that the core field is dominant for spherical harmonic degrees 1 to 12 and the lithospheric field is dominant for degrees larger than 16, with both sources contributing comparably at degrees 13 to 15 [1]. Maus et al. [11] used the model Ørsted-06a-01 and subtracted the core field up to degree 14 from CHAMP magnetic data. Thébault et al. [15] used the DCO (Dedicated core field model, up to degree 18) to correct for the core field when dealing with the Swarm magnetic data.

The field models IGRF (up to degree 13) and WMM (up to degree 12) are widely used in a variety of areas, but are of limited use for the purpose of properly extracting lithospheric field from satellite magnetic data. The CHAOS-7 model [20] is based on satellite data from the Ørsted, CHAMP, SAC-C, Cryosat-2 and the three Swarm satellites, as well as monthly mean ground observatory secular variation data. It describes the core field, the large-scale external field and its induced counterpart, and the lithospheric field (see http://www.spacecenter.dk/files/magnetic-models/CHAOS-7 for model coefficients). In the CHAOS-7 model, the core field extends formally to degree 20. We used the CHAOS-7 model to remove the field up to degree 20 from the CSES scalar data.

3.3 External field removal

Dealing with the external field is the biggest challenge to properly extract the lithospheric field signal [11]. The external field is caused by currents in the ionosphere and magnetosphere. By selecting night-side quiet time satellite data, the influence of ionospheric contributions is effectively reduced, but not that of magnetospheric signals. Ravat et al. [6] applied along-track high-pass filter to remove these remaining magnetospheric field contributions. Maus et al. [11] used the standard D_{st} correction and further subtracted a first order estimate of external field. Thébault et al. [15] subtracted a magnetospheric model to degree 1 and then introduced additional processing by removing an along-track fitting of an external magnetic dipole.

The CHAOS model series provides not only the core field but also the external and lithospheric field [20,27]. In this study, the CHAOS-7 model [20,27] is used to subtract the external field up to degree 2, parameterized by the RC (Ring Current) index to provide an improved description of the magnetospheric field (in particular during quiet conditions) compared to D_{st} [28].

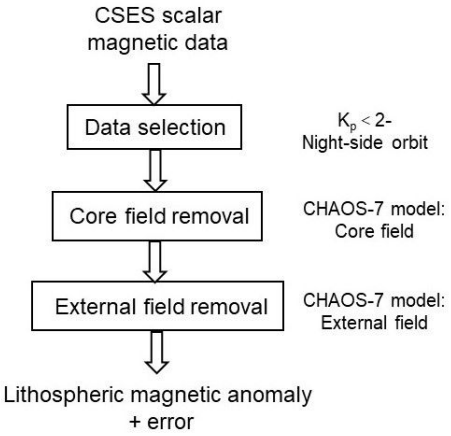

Figure 2 Flowchart of along-track processing of CSES scalar magnetic data.

4 . Along-track analysis of the lithospheric magnetic anomaly

Two regions with large-scale magnetic anomalies, the Bangui and Tarim magnetic anomalies, are first chosen to perform an along-track analysis of CSES scalar magnetic data. The results show that CSES data reveal the lithospheric magnetic anomaly clearly. The locations of five chosen orbits are shown in Figure 3: Orbits 1 and 2 cross the Bangui magnetic anomaly (BMA), Orbits 3 and 4 cross the Tarim magnetic anomaly (TMA), while Orbit 0, above the Atlantic ocean, does not show any significant magnetic anomaly at the corresponding latitudes and is included for reference. The underlying map of Figure 3 shows the total-intensity (scalar) magnetic anomaly computed from the CHAOS-7 model for spherical harmonic degrees between 21 and 110 at 507 km altitude above a sphere of radius 6371.2 km, i.e., the average altitude of CSES orbits.

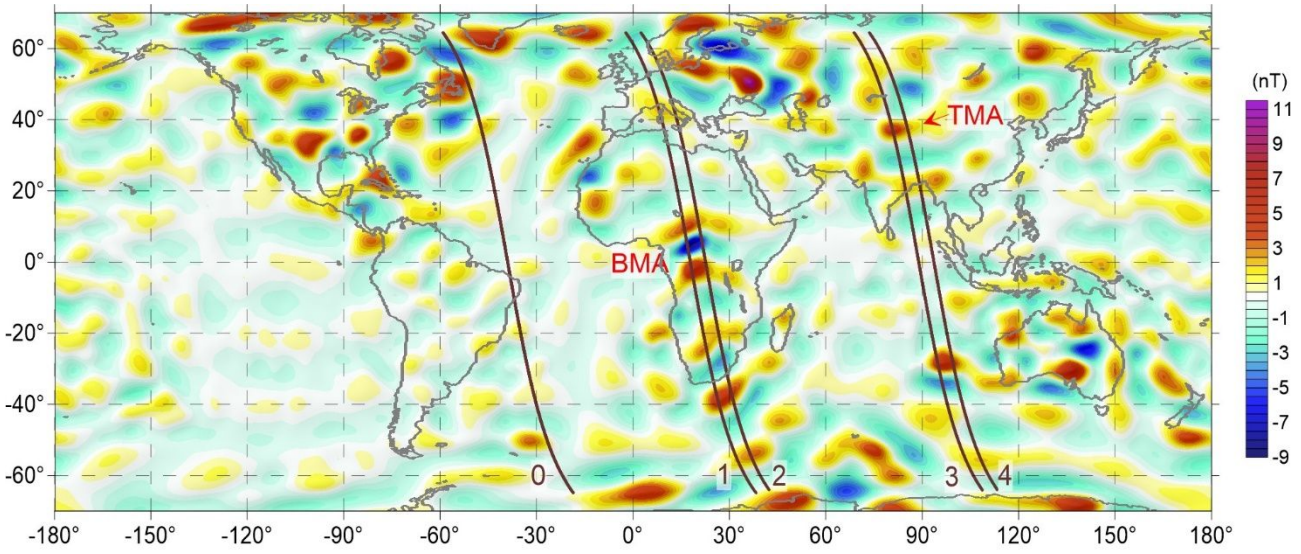

Figure 3 Locations of five chosen orbits for along-track analysis in this study. The underlying map shows the total-intensity (scalar) magnetic anomaly computed from the CHAOS-7 model at 507 km altitude (http://www.spacecenter.dk/files/magnetic-models/CHAOS-7/index.html). Orbit 0: taken as a reference with no significant anomaly at the latitude of BMA; Orbit 1 and 2: above BMA (Bangui magnetic anomaly); Orbit 3 and 4: above TMA (Tarim magnetic anomaly).

4.1 Bangui magnetic anomaly (BMA)

The BMA in central Africa is well known as one of the largest magnetic anomalies on Earth (Figure 3). Its center is a prominent magnetic low located at 5 °N latitude. It is in an area of highly metamorphic Precambrian rocks, and does not correlate with any surficial features. Combined with other geophysical and geological data, it was interpreted to be caused by early intrusions in the crust and followed by subsidence and deformation [3].

In Figure 4(a), after removing the core and external field CHAOS-7 model, the magnetic data of Orbits 1 and 2 both clearly reveal the magnetic low of BMA at 5°N. Figure 4(a) also shows the residual magnetic data if only the core field is removed, to illustrate the influence of external fields. The magnetic data after removing both core and external fields have lower variances than those after just removing the core field. To further highlight this BMA signature, we extracted Orbit 0, which shows no significant magnetic anomaly at 5 ° N latitude, for comparison with the two orbits above BMA. After removing core and external fields, the magnetic data of Orbit 0 indeed show no anomaly at the corresponding latitude of BMA.

Figure 4(b) shows the scalar magnetic anomaly data for six revisiting tracks of Orbit 1. In theory, if there were no sources other than the lithospheric sources, the residual magnetic data after processing would be identical for all tracks. After removing the core field, however, the amplitude of these residual magnetic data (shown as red curves) still cover a wide range of values and reaches -35 nT at 5°N. After further removing the external field, the magnetic anomaly data (shown as blue curves), have smaller variances, and are much more consistent with the lithospheric magnetic anomaly (green curve) as computed from CHAOS-7 for spherical harmonic degrees 21 to 110. The BMA now shows a clear signature with a central minimum of -10 nT and side maxima of 5 nT. In the along-track magnetic data, the differences between the red and blue curves indicate that the influence of external field acts as gently changing trends superposed on the time-independent lithospheric field. This illustrates that effective removal of the external field is essential for lithospheric field studies.

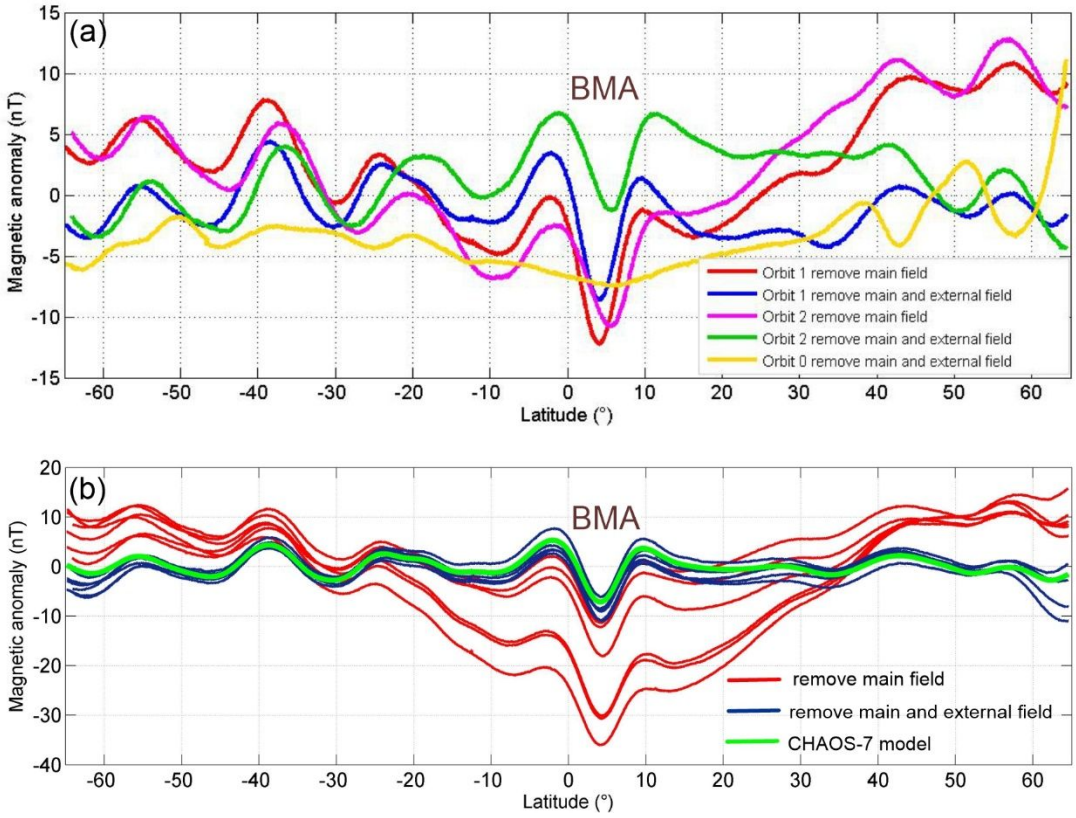

Figure 4 Magnetic anomaly of the BMA at 5°N. (a) Magnetic anomaly along two orbits that cross the BMA area. Orbits 1 (Track 08311 on 3 August 2019) and 2 (Track number 08326 on 4 August 2019) cross the BMA area, and are compared to Orbit 0 (Track 08283 on 1 August 2019) which does not cross this area and has no significant anomaly at the corresponding latitude. (b) Magnetic anomaly of six revisiting tracks of the Orbit 1 (Tracks 08311 on 3 August 2019, 08387 on 8 August 2019, 08615 on 23 August 2019, 08843 on 7 September 2019, 08919 on 12 September 2019 and 09147 on 27 September 2019). The local time is the same for all these night-side tracks (descending node at 02:00).

4.2 Tarim magnetic anomaly (TMA)

TMA is one of the most significant magnetic anomalies in China, and is characterized by a magnetic high centered on 38°N. In Figure 5(a), after removing the core and external fields as described by the CHAOS-7 model, the magnetic data of Orbits 3 and 4 both clearly reveal the magnetic high of TMA at 38°N. Figure 5(a) also shows the residual magnetic data of Orbits 3 and 4 when just removing the core field.

Figure 5(b) shows the magnetic anomaly data of six revisiting tracks of Orbit 3. The magnetic data after removing the core field are shown as red curves. The magnetic anomaly data after removing core and external field (blue curves) have smaller variances, and are consistent with the lithospheric magnetic anomaly (green curve) computed from CHAOS-7 model for spherical harmonic degrees 21 to 110. The amplitude of TMA at CSES altitude ranges from 0 to 5 nT. Along these orbits, there is another significant lithospheric magnetic anomaly at 28° S, which is also consistent with what is seen in the CHAOS-7 model (recall Figure 3). At 60°S, the magnetic data

after removing core and external fields show obvious inconsistencies, which indicates that high-latitude data are more influenced by the magnetic disturbances due to polar electric currents, which we did not correct for.

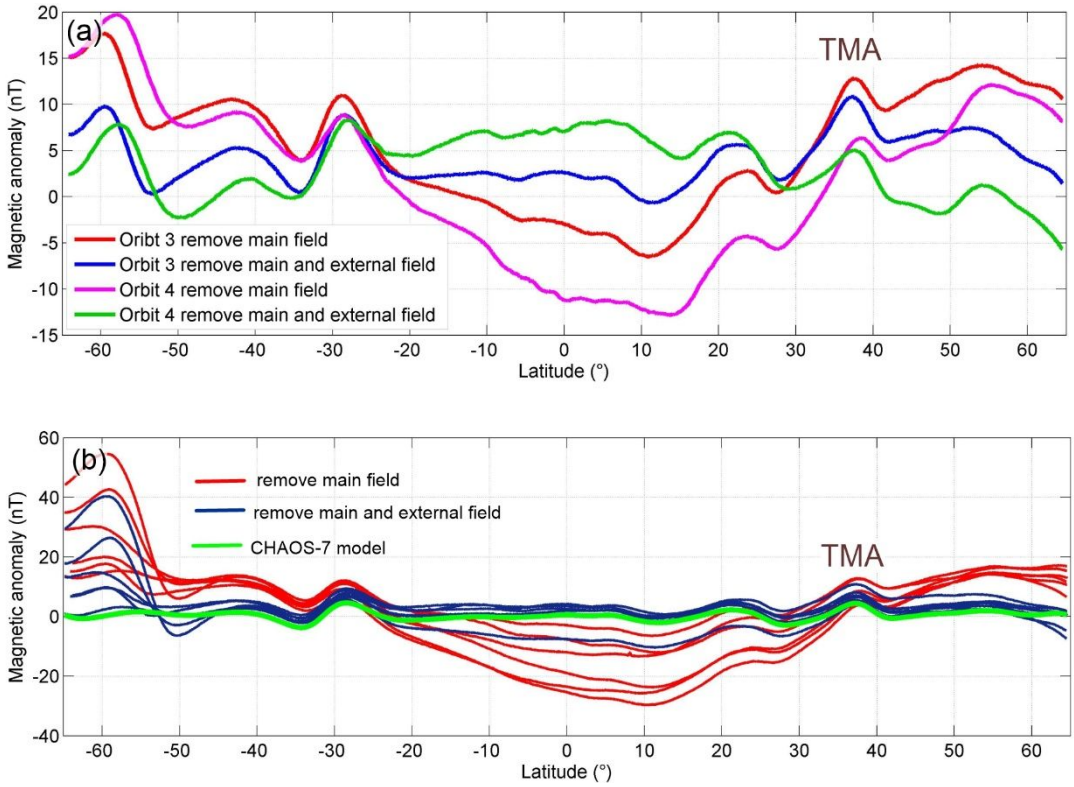

Figure 5 Magnetic anomaly of the TMA at 38°N (a) Magnetic anomaly along two orbits that cross the TMA aera: Orbits 3 (track number 08308 on 1 August 2019) and 4 (Track number 08703, 28 August 2019). (b) Magnetic anomaly of six revisiting tracks of the Orbit 3 (Tracks 08308 on 2 August 2019, 08384 on 7 August 2019, 08460 on 12 August 2019, 08916 on 11 September 2019, 09068 on 21 September 2019 and 09144 on 26 September 2019). The local time of these night-side orbits is the same for all these night-side tracks (descending node at 02:00).

5 . Lithospheric magnetic anomaly map for China and surrounding regions

In the Chinese region, three magnetic high anomalies and one magnetic low anomaly are noticeable at CSES altitude [10, 29-31]. The three magnetic high anomalies are located near the Tarim basin (in northwest of China), near the Sichuan basin (in southwest of China) and near the Songliao basin (in northeast of China). A broad magnetic low is found above the southern part of the Himalayan-Tibetan plateau. In this study, two months (August to September 2019) of CSES magnetic data are used to compile an initial lithospheric magnetic anomaly map of China and surrounding regions. For each orbit, the data with the smallest K_p (< 1) are now chosen and processed to remove the core and external field as described in sections 3.2 and 3.3. We next use line leveling and gridding (neglecting altitude variations by assuming a constant altitude of 507 km for all measurements). The line leveling is to eliminate the differences of background values between lines. During leveling and for each repeating orbit, a reference line is first selected (by fitting a quadratic polynomial to each line and selecting the line with the least variations in this polynomial, which we assume reflect the level of remaining non-lithospheric signal contamination) and the values of other lines are next corrected by subtracting a constant value to best fit the data of the

corresponding reference line. Then, to produce a grid map, the Kriging gridding method integrated in the Surfer® software (version 13, see https://www.goldensoftware.com/products/surfer) is used. The root mean square between the real data and gridding data then is 0.0424 nT. Figure 6(a) shows the resulting map on a grid with 0.2° spacing. The three magnetic high anomalies in the Tarim, Sichuan and Songliao basins, and the magnetic low in the southern Himalayan-Tibetan plateau are all clearly revealed.

5.1 Comparison with CHAOS model

To further assess the above CSES results, we compare the lithospheric magnetic anomaly map (Figure 6a) with a similar map calculated from the CHAOS-7 model at the same altitude of 507 km, using spherical harmonic degrees between 21 and 110 plotted on a similar grid with 0.2° spacing (Figure 6b). The centers and trends of the four magnetic anomalies almost coincide. In details, however, the magnetic anomalies in the two maps show differences in shape and distribution. For example, the east-west trending Tarim magnetic anomaly in the CSES result is much broader than in the CHAOS-7 model, and the eastern part of Tarim magnetic anomaly (TMA) has lower amplitude and shows two branches in the CHAOS-7 map, not seen in the CSES map. The total amplitude range of the anomaly maps is 9 nT, from -4 to 5 nT in the case of CSES, from -4.5 to 4.5 nT for CHAOS-7. These differences are likely caused by the different data processing strategies, such as external field removal or data leveling, which can influence the result by introducing biases during processing. Overall, however, the initial lithospheric magnetic anomaly map derived from CSES data over China and surrounding regions is consistent with the one derived from the CHAOS-7 model and reveals similar anomaly amplitudes and distribution.

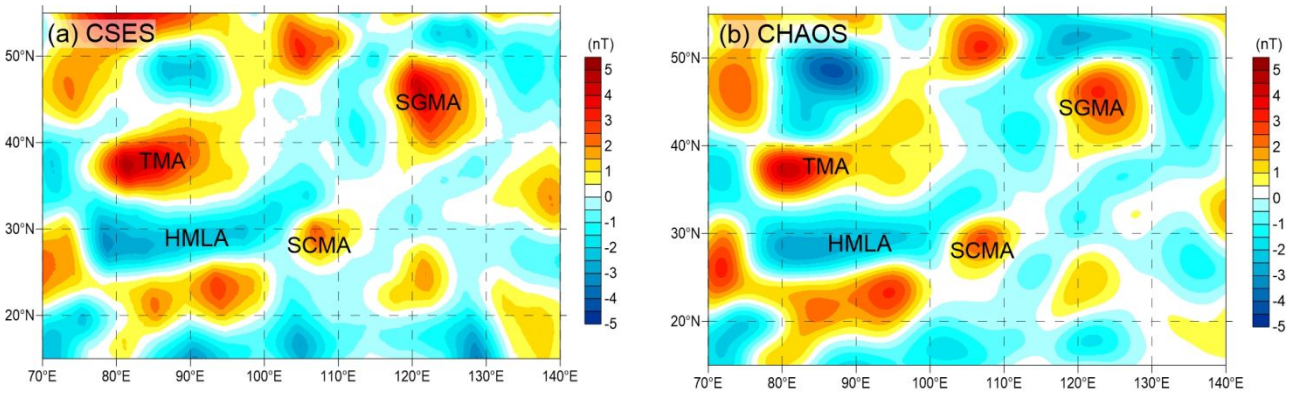

Figure 6 Lithospheric magnetic anomaly map over China and surrounding regions at average 507 km altitude (a) derived from CSES data (with amplitudes ranging from -4 to 5 nT) and (b) given by the CHAOS-7 model (with amplitude ranging from -4.5 to 4.5 nT). The same color code with amplitudes ranging from -5 to 5 nT is used. Abbreviations: TMA, Tarim magnetic high anomaly; SCMA, Sichuan magnetic high anomaly; SGMA, Songliao-Greater Khingan magnetic high anomaly; HMLA, Himalayan-Tibetan magnetic low anomaly.

5.2 Geological origins

Long-wavelength magnetic anomalies obtained by satellites originate from large or deep sources beneath the surface, and their formations are always related to large-scale tectonic-magmatic activity. Aeromagnetic anomalies show the short-middle wavelength signals with more details and have more direct connections to the geology at the surface [32,33]. Here, the findings from these aeromagnetic data are discussed jointly with those of the CSES magnetic anomaly map to analyze the geological origins of the long-wavelength magnetic anomalies identified

above.

The Tarim magnetic anomaly (TMA) is the largest one in the region. But the basement of Tarim basin is mostly covered by non-magnetic desert and no highly-magnetized rocks is exposed at the surface. The distribution of the Tarim basin anomaly as seen in aeromagnetic data [34] is compatible with what is seen in the satellite data. The aeromagnetic anomaly in Tarim basin reflects the magnetization difference of the basement, and its geological origin has been related to multi-stage magmatism during geological history [34,35].

The Sichuan magnetic anomaly (SCMA) is smaller in scale than the Tarim magnetic anomaly, but its geological setting is quite similar. The Sichuan basin is covered by thick non-magnetic sedimentary layers from Neoproterozoic to Cenozoic, which conceals the Precambrian basement where the sources lie. Wang et al. [36] performed a 3D inversion of the aeromagnetic data and compared the results with geological maps. They proposed that the geological origin of the Sichuan Basin magnetic anomaly be related to the craton-scale Neoproterozoic magmatic event, which has played an important role in the stabilization of the basement and the evolution of the deep crust below the Sichuan Basin.

The Songliao magnetic anomaly (SGMA) is located in the area of the Greater Khingan range and Songliao basin at the northeast of China, with a center close to the Greater Khingan range. The distribution of aeromagnetic anomaly in this area is related to the exposed igneous rocks in Greater Khingan range formed by intense magmatic activities during the Mesozoic period. The magnetic anomaly extends to the Songliao basin, which is covered by sedimentary layers. To clarify its geological origin, further quantitative analysis of the aeromagnetic anomaly would be needed.

The magnetic low in the southern Himalayan-Tibetan plateau (HMLA) has a wide spatial range. It is elongated along the east-west direction and is near-parallel to the mainly east-west trending tectonic sutures due to the north-south subduction and collision in the Himalayan-Tibetan plateau region. The aeromagnetic anomalies in southern Tibet are of relatively small spatial scales, generally along the east-west sutures and related to the magmatic arcs and ophiolites formed during the subduction and collision [37]. Their magnetic signature in southern Tibet attenuates quickly with altitude, and thus has no obvious relation to the broad satellite magnetic low. The formation of this wide magnetic low anomaly is considered to be caused by the high heat flow and shallow Curie depth below the southern Himalayan-Tibetan plateau [38,39].

6 . Concluding Remarks

Along-track analysis of scalar magnetic data obtained by the CSES satellite demonstrates that CSES magnetic data are sensitive to lithospheric magnetic anomalies, which indicates that the CSES satellite delivers high-quality magnetic data for geophysical and geological studies.

1 . An initial lithospheric magnetic anomaly map for the Chinese region is obtained and shown to be generally consistent with the lithospheric magnetic anomaly as given by the CHAOS-7 model. There are some small differences in anomaly amplitude and spatial distribution due to data processing and some remaining influence of the external field. To further improve global magnetic anomaly maps derived from CSES magnetic data, more work is needed. This would involve, in particular, choosing more suitable data selection criterion for the whole data set, better modeling residual external magnetic fields, as well as improving data leveling and spherical harmonic analysis.

2 . The distribution of magnetic anomalies as seen in the CSES data can be used jointly with aeromagnetic maps to discuss the geological origins of the four major long-wavelength magnetic anomalies we found over China and surrounding regions. Three magnetic high anomalies, located near Tarim, Sichuan and Songliao, are all associated with major basins in China, and their formations are always related to

large-scale tectonic magmatic activities during geological history. A prominent magnetic low in the southern Himalayan-Tibetan plateau is related to the shallow Curie depth in that region, which causes thinner magnetized layers compared to other places.

3. The geomagnetic field comprises contributions from various sources, including the core field, the lithospheric field, the external field, as well as contributions from secondary, electromagnetic induced currents in the crust and mantle, and ocean-generated fields. It can be used for basic research and application, e.g. for navigation. For scientific investigations of other sources, the magnetic signature of the lithosphere should be removed. Navigation also calls for high-precision knowledge of the regional lithospheric field. To improve model accuracy, the various data sources (satellite, airborne and ground observations) should be combined, and data fusion technology and robustness analysis would be important during further geomagnetic modeling.

Financial support

This work was supported by the China Postdoctoral Science Foundation [grant number 2019M660731], the National Key R&D (Research and Development) Program of China [grant number 2018YFC1503500] and ISSI-BJ (International Space Science Institute-Beijing) [grant number 2019IT-33]. Work by GH and NO is supported as part of *Swarm* DISC activities, funded by ESA [grant number 4000109587]. Work by ADS is supported by LIMADOU-Science Project, funded by ASI (Italian Space Agency). Work of WM is supported by the Austrian Space Applications Programme [grant number 873688].

Acknowledgements

This work made use of the data from CSES mission (http://leos.ac.cn), a project funded by the China National Space Administration (CNSA) and the China Earthquake Administration (CEA).

References

1 Langel R A, Hinze W J. The Magnetic Field of the Earth's Lithosphere: The Satellite Perspective. 1998, Cambridge University Press: Oxford.

2 Ferré E C, Friedman S A, Martín-Hernández F, et al. Eight good reasons why the uppermost mantle could be magnetic. Tectonophysics, 2014, 624-625:3-14.

3 Regan R D, Marsh B D. The Bangui magnetic anomaly: its geological origin. Journal of Geophysical Research, 1982, 87:1107-1120.

4 Pilkington M, Saltus R W. The Mackenzie River magnetic anomaly, Yukon and Northwest Territories, Canada-Evidence for Early Proterozoic magmatic arc crust at the edge of the North American craton. Tectonophysics, 2009, 478:78–86.

5 Hinze W J, Allen D J, Fox A J, et al. Geophysical investigations and crustal structure of the North American Midcontinent Rift system. Tectonophysics, 1992, 213:17-32.

6 Ravat D, Langel R A, Purucker M, et al. Global vector and scalar Magsat magnetic anomaly maps. Journal of Geophysical Research, 1995, 100(B10):20111.

7 Regan R D, Cain J C, Davis W M. A Global Magnetic Anomaly Map. Journal of Geophysical Research, 1975, 80(5).

8 Arkani-Hamed J, Langel R A, Purucker M. Scalar magnetic anomaly maps of Earth derived from POGO and Magsat data. Journal of Geophysical Research, 1994, 99(B12).

9 Purucker M, Langlais B, Olsen N, et al. The southern edge of cratonic North America: Evidence from new satellite magnetometer observations. Geophysical Research Letters, 2002, 29(15): 8000.

10 Hemant K, Maus S. Geological modeling of the new CHAMP magnetic anomaly maps using a geographical information system technique. Journal of Geophysical Research: Solid Earth, 2005, 110(12):1-23.
11 Maus S, Rother M, Holme R, et al. First scalar magnetic anomaly map from CHAMP satellite data indicates weak lithospheric field. Geophysical Research Letters, 2002, 29(14):1702.
12 Maus S, Rother M, Hemant K, et al. Earth's lithospheric magnetic field determined to spherical harmonic degree 90 from CHAMP satellite measurements. Geophysical Journal International, 2006, 164(2):319-330.
13 Maus S, Lühr H, Rother M, et al. Fifth-generation lithospheric magnetic field model from CHAMP satellite measurements. Geochemistry, Geophysics and Geosystems, 2007, 8(5).
14 Friis-Christensen E, Lühr H and Hulot G. Swarm: A constellation to study the Earth's magnetic field, Earth, Planets and Space, 2006, 58:351-358.
15 Thébault E, Vigneron P, Langlais B, et al. A Swarm lithospheric magnetic field model to SH degree 80 Swarm Science Results after two years in Space 1. Geomagnetism. Earth, Planets and Space, 2016, 68(1).
16 Olsen N, Ravat D, Finlay C C, et al. LCS-1: A high-resolution global model of the lithospheric magnetic field derived from CHAMP and Swarm satellite observations. Geophysical Journal International, 2017, 211(3):1461-1477.
17 Shen X H, Zhang X M, Yuan S G, et al. The state-of-the-art of the China Seismo-Electromagnetic Satellite mission. Science China: Technological Sciences, 2018, 61(5):634-642.
18 Huang J, Shen X, Zhang X, et al. Application system and data description of the China Seismo-Electromagnetic Satellite. Earth and Planetary Physics, 2018, 2(6):444-454.
19 Yang Y, Hulot G, Vigneron P, et al. The CSES Global Geomagnetic Field Model (CGGM): An IGRF type global geomagnetic field model based on data from the China Seismo-Electromagnetic Satellite. Earth, Planets and Space, 2020. (under review)
20 Finlay C C, C Kloss, N Olsen et al. The CHAOS-7 geomagnetic field model and observed changes in the South Atlantic Anomaly. Earth, Planets and Space, 2020, under review.
21 Thébault E, Purucker M, Whaler K A, et al. The magnetic field of the earth's lithosphere. Space Science Reviews, 2010, 155(1-4):95-127.
22 Pollinger A, Lammegger L, Magnes W, et al. Coupled Dark State Magnetometer for the China Seismo-Electromagnetic Satellite. Measurement Science and Technology, 2018, 29: 095103 (10pp).
23 Pollinger A, Amtmann C, Betzler A et al. In-orbit results of the Coupled Dark State Magnetometer aboard the China Seismo-Electromagnetic Satellite. Geoscientific Instrumentation Methods and Data Systems, 2020, 9: 275-291.
24 Cheng B J, Zhou B, Magnes W, et al. High precision magnetometer for geomagnetic exploration onboard of the China Seismo-Electromagnetic Satellite. Science China: Technological Sciences, 2018, 61(5):659-668.
25 Zhou B, Yang Y, Zhang Y, et al. Magnetic field data processing methods of the China Seismo-Electromagnetic Satellite. Earth and Planetary Physics, 2018, 2(6):455-461.
26 Zhou B, Cheng B, Gou X, et al. First in-orbit results of the vector magnetic field measurement of the High Precision Magnetometer onboard the China Seismo-Electromagnetic Satellite. Earth, Planets and Space, 2019, 71: 119.
27 Finlay C C, Olsen N, Kotsiaros S, et al. Recent geomagnetic secular variation from Swarm and ground observatories as estimated in the CHAOS-6 geomagnetic field model. Earth, Planets and Space, 2016, 68(1):1-18.
28 Olsen N, Lühr H, Finlay C C, et al. The CHAOS-4 geomagnetic field model. Geophys J Int. 2014;197(2):815-827.
29 Arkani-Hamed J, Zhao S K, Strangway D W. Geophysical interpretation of the magnetic anomalies of China

derived from Magsat data. Geophysical Journal, 1988, 95(2):347-359.

30 Zhang C D. Deduction of magnetic characteristics of lithosphere in China from results on satellite and aeromagnetic measurements. Progress in Geophysics, 2003, 18(1):103-110. (in Chinese with English abstract)

31 Kang G F, Gao G M, Bai C H, et al. Distribution of the magnetic anomaly for the CHAMP satellite in China and adjacent areas. Chinese Journal of Geophysics, 2010, 53(4):895-903. (in Chinese with English abstract)

32 Xiong S. Q, Jing T, Ding Y Y, et al. Aeromagnetic data and geological structure of continental China: A review. Applied Geophysics, 2016a, 13: 227-237.

33 Xiong, S., Yang, H., Ding, Y., et al. Distribution of igneous rocks in China revealed by aeromagnetic data. Journal of Asian Earth Sciences, 2016b, 129, 231–242.

34 Wu G H, Li H W, Xu Y L, et al. The tectonothermal events, architecture and evolution of Tarim craton basement palaeo-uplifts. Acta Petrologica Sinica, 2012, 28(8):2435-2452.

35 Gao G, Kang G, Bai C, et al. Distribution of the crustal magnetic anomaly and geological structure in Xinjiang, China. Journal of Asian Earth Sciences, 2013, 77:12-20.

36 Wang J, Yao C, Li Z, et al. 3D inversion of the Sichuan Basin magnetic anomaly in South China and its geological significance. Earth, Planets and Space, 2020a, 72:40.

37 Wang J, Yao C, Li Z. Aeromagnetic Anomalies in Central Yarlung-Zangbo Suture Zone (Southern Tibet) and Their Geological Origins. Journal of Geophysical Research: Solid Earth, 2020b, 125(2):1-24.

38 Hemant K, Mitchell A. Magnetic field modelling and interpretation of the Himalayan-Tibetan Plateau and adjoining north Indian Plains. Tectonophysics, 2009, 478. 87-99.

39 Qiu Y, Wang Z, Jiang W, et al. Combining CHAMP and swarm satellite data to invert the lithospheric magnetic field in the Tibetan Plateau. Sensors, 2017, 17(2).